J. Fluid Mech. (2026), *vol.* 1040, R1, doi:10.1017/jfm.2026.11885



Feedthrough between two successive cylindrical water–air interfaces in divergent geometry

Shuzhen Niu[1], **Pengfei Yang**[1,2], **Baoqing Meng**[1,2] **and Yu Liang**[1,2]

[1]State Key Laboratory of High Temperature Gas Dynamics, Institute of Mechanics, Chinese Academy of Sciences, Beijing 100190, PR China

[2]School of Engineering Science, University of Chinese Academy of Sciences, Beijing 100049, PR China

Corresponding author: Yu Liang, liangyu@imech.ac.cn

(Received 13 April 2026 UTC; revised 18 June 2026 UTC; accepted 3 July 2026 UTC)

This study experimentally and theoretically investigates the feedthrough between two successive cylindrical water–air interfaces under divergent expansion. Three initial conditions are examined: interfaces initially in-phase and anti-phase, and an initially unperturbed outer interface. Amplitude measurements reveal that the feedthrough depends on the initial perturbation phase difference, thereby altering the instability evolution of both interfaces. A linear theory is developed for cylindrical fluid layers, accounting for surface tension and cylindrically divergent (outward-expanding) geometry, and agrees well with experiments in the near-unity Atwood number regime. Dimensionless feedthrough efficiency factors derived from the linear theory demonstrate that the interface coupling is determined by the radius ratio of two interfaces, interface acceleration, and perturbation wavenumbers. Notably, under extremely high acceleration (as a theoretical limit of our model), the feedthrough is predicted to stabilise both interfaces. This trend, if it persists under compressible conditions, could have implications for inertial confinement fusion. These results provide critical guidance for instability manipulation in both radially convergent and radially divergent geometries.

Key words: instability, gas/liquid flow

1. Introduction

When a heavier fluid is accelerated by a lighter one, the interface becomes susceptible to Rayleigh–Taylor instability (RTI) (Rayleigh 1883; Taylor 1950). This instability, driven by density mismatch and effective acceleration, is of fundamental importance in inertial confinement fusion (ICF) (Lindl *et al.* 2014; Zhou *et al.* 2025), astrophysical phenomena such as supernovae (Müller 2020), and various industrial processes in cylindrical and spherical geometries. In the present study, we consider a divergent

© The Author(s), 2026. Published by Cambridge University Press.

https://doi.org/10.1017/jfm.2026.11885 Published online by Cambridge University Press

cylindrical configuration, i.e. the interfaces move radially outwards, in contrast to convergent (imploding) geometries often studied in ICF. More specifically, radially expanding cylindrical liquid layers are encountered in inkjet printing (where annular jets undergo break-up), industrial spray atomisation, liquid curtains for dust suppression, and pressure-driven flows in liquid-lined cylindrical vessels. However, in many realistic situations, material layers have finite thickness, and two interfaces exist in close proximity. The perturbation on one interface can influence the evolution of the other through the pressure and velocity fields in a finite-thickness layer – a coupling mechanism known as feedthrough (Mikaelian 2025). Understanding feedthrough in such divergent liquid–air interfaces can guide the control of interfacial instabilities in these applications.

Taylor (1950) first studied the linear development of RTI for a single fluid layer accelerated in vacuum. Goncharov *et al.* (2000) considered compressibility and analysed RTI growth in finite-thickness fluid layers across different geometries. Ryutov & Dorf (2014) investigated RTI growth in a cylindrical shell geometry, including the effect of a magnetic field. Weis *et al.* (2015) also studied RTI development at a shell interface in a cylindrical geometry in the presence of a magnetic field. Mikaelian (1982*a*,*b*) examined the linear RTI growth rates at $N-1$ interfaces in a system of N fluids, and argued that any arbitrary density transition layer can be approximated by a large number of finite-thickness fluid layers. However, as the number of fluid interfaces increases, obtaining an analytical expression for the perturbation growth rate becomes difficult. Wang *et al.* (2014) developed a weakly nonlinear model, and showed that the layer thickness dominates the perturbation evolution when the normalised thickness is $kd < 1$, where k and d are the wavenumber and layer thickness, respectively. More recently, Mikaelian (2025) defined feedthrough efficiency factors for RTI and Richtmyer–Meshkov instability (RMI), demonstrating that the feedthrough is stronger in RMI than in RTI, and further exploring how it can be exploited to suppress instabilities. Recently, Yuan *et al.* (2023, 2024) extended linear stability analyses for cylindrical fluid layers in vacuum to arbitrary Atwood numbers, considering thin-shell corrections and interface coupling effects in shock-accelerated configurations. They found that the Atwood number and the initial phase difference between the two interfaces of a thin shell have a non-negligible influence on interfacial instabilities. These studies collectively show that finite-thickness effects not only modify the growth rate of a single interface, but more importantly, allow perturbations on one interface to feed through the layer to the other.

The geometry of the interface plays a crucial role on the instability development. The ICF capsules are spherical, supernova ejecta are shell-like, and many experimental set-ups adopt cylindrical configurations to combine convergence effects with optical accessibility. Bell (1951) first analysed Taylor instability on cylinders and spheres in the small-amplitude regime, and Plesset (1954) systematically studied interface stability in converging geometries, laying the foundation of the Bell–Plesset effect. This effect indicates that even in the absence of classical RTI acceleration, radial convergence or divergence of an interface amplifies (or suppresses) initial perturbations. Epstein (2004) noted that 'undriven growth' more accurately describes convergence and compression effects in the absence of buoyancy-driven RTI. Recent high-energy-density experiments have provided valuable insights into cylindrical RTI and feedthrough. Sauppe *et al.* (2020) demonstrated scale-invariant RTI growth in laser-driven convergent cylindrical implosions, showing that the instability evolves self-similarly for targets scaled by a factor of three, highlighting the importance of cylindrical convergence effects on RTI. In the context of feedthrough, Merritt *et al.* (2024) developed a quantitative radiography technique to measure density fluctuations and mixing parameters in a thin-layer RMI experiment under planar shock–reshock conditions. Together, these studies

https://doi.org/10.1017/jfm.2026.11885 Published online by Cambridge University Press

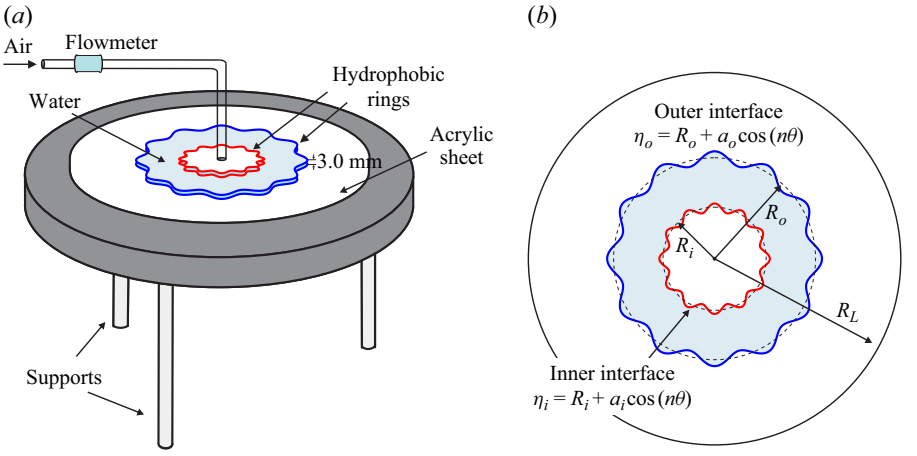


Figure 1. (*a*) Experimental set-up schematic. (*b*) Initial interface configuration.

underscore the broad relevance of interface coupling and cylindrical geometry to ICF, and they complement our investigation by covering different acceleration regimes and geometries. Most existing studies have focused on the RTI and RMI of gaseous interfaces (Weir *et al.* 1998; Ding *et al.* 2017), while studies on the RTI of multiphase interfaces remain scarce. The presence of a multiphase interface, such as a liquid–gas interface, introduces surface tension and viscosity effects (Liang & Luo 2025, 2026). Furthermore, a natural and important question arises: how does feedthrough behave when a finite-thickness layer possesses two curved liquid–air interfaces in a cylindrical configuration?

This study fills this gap through combined experimental and theoretical investigation of a cylindrically divergent water layer. We utilise hydrophobic-coated rings to create a thin water layer with controllable initial conditions. We derive coupled evolution equations for the two interface perturbations, analyse how cylindrical divergence modulates feedthrough efficiency, and quantify its dependence on physical parameters.

2. Experimental method

The experiment was conducted in a device comprising two transparent acrylic sheets (spacing $h = 3.0$ mm, radius $R_L = 200.0$ mm), as shown in figure 1(*a*). A 4.0 mm diameter hole was drilled at the centre of the top sheet. Two pairs of precisely machined micro-channels (width 1.0 mm, depth 2.0 mm) with single-mode patterns were engraved on opposing surfaces (marked in red and blue), into which hydrophobic-coated acrylic rings (width 0.9 mm, height 2.0 mm) were embedded to constrain the inner and outer water–air interfaces. The single-mode micro-channels are positioned at inner radius $R_i^0 = 25.0$ mm and outer radius $R_o^0 = 33.0$ mm. The hydrophobic-coated rings increase the water–air interface contact angle (typically $> 90°$), enabling precise control of the interface geometry. The hydrophobic rings serve not only to pin the contact lines, but also to prescribe the initial conditions on the two interfaces. Changing the ring geometry (e.g. width or shape) would alter the achievable initial radii and wavenumbers, which in turn significantly affect the instability evolution (Liang & Luo 2025, 2026). Contact line pinning inevitably introduces a slight three-dimensionality, including a thicker interface contour and a weak Poiseuille-type flow in the direction perpendicular to the acrylic plates. However, the width of the interface contour caused by pinning is much smaller than the expanding radius of the interface. Hence the two-dimensional governing equations remain

https://doi.org/10.1017/jfm.2026.11885 Published online by Cambridge University Press

Case	n	R_i^0 (mm)	R_o^0 (mm)	a_i^0 (mm)	a_o^0 (mm)	$\lvert na_i^0/2\pi R_i^0\rvert$	$\lvert na_o^0/2\pi R_o^0\rvert$
IP	12	25.0	33.0	1.0	1.0	0.076	0.058
UP	12	25.0	33.0	1.0	0	0.076	0
AP	12	25.0	33.0	1.0	−1.0	0.076	0.058

Table 1. Initial interface parameters, where n denotes the azimuthal wavenumber, R_i^0 and R_o^0 denote the initial radii of the inner and outer interfaces, respectively, and a_i^0 and a_o^0 denote the initial amplitudes of the inner and outer interfaces, respectively.

a good approximation for the dominant instability dynamics. Before experiments, the space between the inner and outer single-mode rings was filled with pure water (dyed in cyan). At the start of the experiments, high-pressure air was suddenly injected through the top hole at $25\,\mathrm{l\,min^{-1}}$ regulated by a flowmeter via a cable.

The initial single-mode perturbations on the inner interface (η_i) and outer interface (η_o) in polar coordinates are given by

$$\eta_i^0 = R_i^0 + a_i^0\cos(n\theta), \quad \eta_o^0 = R_o + a_o^0\cos(n\theta), \tag{2.1}$$

where a_i^0 and a_o^0 are the initial amplitudes of the inner and outer interfaces, respectively, n is the azimuthal wavenumber, and θ is the angle. Table 1 lists the initial parameters for all cases, where the initial conditions are interfaces initially in-phase (IP) and anti-phase (AP), and an initially unperturbed outer interface (UP). The initial amplitude-to-wavelength ratios are all within 0.1, ensuring that the evolution remains in the linear regime initially. A high-speed camera (FASTCAM MINI WX; 1000 fps, 0.25 ms shutter) captured the flow at resolution $0.067\,\mathrm{mm\,pixel^{-1}}$, with backscatter illumination. The ambient pressure and temperature are 101.3 kPa and 293.5 ± 0.5 K, respectively. The surface tension (σ) of the water–air interfaces is $67.5\,\mathrm{mN\,m^{-1}}$ (measured with a Kruss K20 tensiometer). The densities of air (ρ_l) and water (ρ_h) are $1.2\,\mathrm{kg\,m^{-3}}$ and $997.0\,\mathrm{kg\,m^{-3}}$, respectively. The viscosities of air (μ_l) and water (μ_h) are 1.8×10^{-2} mPa s and 1.0 mPa s, respectively. The Atwood numbers of the inner interface $A_i = (\rho_h - \rho_l)/(\rho_h + \rho_l)$ and outer interface $A_o = (\rho_l - \rho_h)/(\rho_h + \rho_l)$ are 0.9976 and −0.9976, respectively. The weighted viscosity coefficient $\nu = (\mu_h + \mu_l)/(\rho_h + \rho_l)$ is $1.02\times10^{-6}\,\mathrm{N\,s\,m^{-2}}$.

Figure 2(a) shows the time-dependent radii of the inner interface R_i and outer interface R_o measured from experiments. The uncertainty in radius measurements is approximately ±1 pixel (0.067 mm) due to the edge detection algorithm. The inner and outer radii of the water layer in the three cases exhibit good repeatability and display a linear growth trend over the experimental duration (20 ms). Dimensionless analysis uses time-dependent Reynolds numbers ($Re_{i/o}$) and Weber numbers ($We_{i/o}$) for the inner/outer interface:

$$Re_{i/o} = \frac{\dot{R}_{i/o}R_{i/o}}{n\nu}, \quad We_{i/o} = \frac{(\rho_h+\rho_l)R_{i/o}}{\sigma n}A_{i/o}^2\dot{R}_{i/o}^2. \tag{2.2}$$

The measured time-dependent Reynolds and Weber numbers are presented in figure 2(b). The Reynolds numbers range from 500 to 800, and the Weber numbers range from 2 to 5. Although $Re \gg 1$ generally indicates negligible viscous effects, our measured Reynolds numbers are well above the critical threshold 256, below which viscosity becomes important for interfacial instability, confirming that the system operates in the inviscid regime (Walchli & Thornber 2017). Conversely, while $We \gg 1$ would typically suggest negligible surface tension effects, our observed Weber numbers 2–5 fall within the transitional regime, where surface tension significantly influences interface dynamics

https://doi.org/10.1017/jfm.2026.11885 Published online by Cambridge University Press

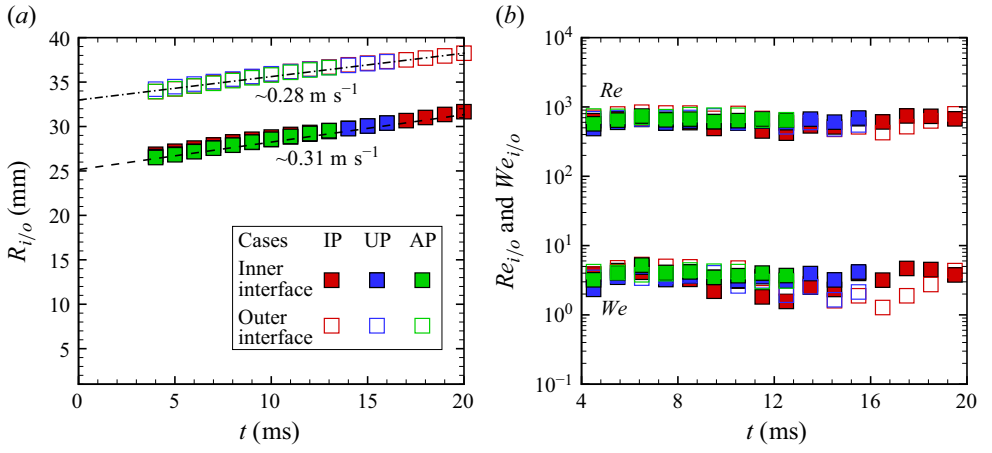


Figure 2. (*a*) Time-dependent radii of the inner interface R_i and outer interface R_o measured from experiments. (*b*) Time-dependent Reynolds numbers ($Re_{i/o}$) and Weber numbers ($We_{i/o}$) for the inner/outer interfaces.

(Hsiang & Faeth 1992). To further assess the influence of boundary layers developing on the acrylic plates, we estimate the laminar displacement thickness $\delta^* = 1.72\sqrt{\nu x/U}$, where $x = 0.0043$ m is the radial displacement of the outer interface at 20 ms in the IP case, $U = \dot{R} \approx 0.28\,\mathrm{m\,s^{-1}}$, and $\nu = \mu_h/\rho_h = 1.0 \times 10^{-6}\,\mathrm{m^2\,s^{-1}}$. This gives $\delta^* \approx 0.21$ mm, which is only 7 % of the gap height (3.0 mm). Therefore, the boundary layers are negligible, and the flow can be treated as inviscid for the purpose of interfacial instability dynamics. In contrast, surface tension plays a significant role in the development of the cylindrical water layer.

3. Results and discussion

Figure 3 illustrates the evolution of successive cylindrically divergent water–air interfaces under various initial conditions. The inner water–air interface is marked in red, and the outer one in blue. During expansion, the perturbation on the inner interface grows because the instability occurs when the lighter fluid (air) pushes against the heavier fluid (water). In contrast, the perturbation on the outer interface is suppressed because the configuration is stable when the heavier fluid (water) pushes against the lighter fluid (air). In the IP and AP cases, the perturbation on the outer interface almost disappears by approximately 12 ms, similar to the UP case where the outer interface is initially unperturbed. Subsequently, the perturbation on the outer interface reverses and becomes prominent at later times, as seen at 20 ms in the IP case. Notably, the bubble–spike symmetry on the inner interface remains largely preserved, whereas the outer interface becomes polygonal, with spikes becoming narrow and sharp, and bubbles becoming wide and flat. This well-defined interface morphology enables precise amplitude measurements via contour analysis.

Owing to the large difference in refractive index between water and air, the interface contour is clearly observable, and the outer edges of the bubble and spike of the outer and inner interfaces can be easily distinguished, as indicated by the blue and red dashed lines in figure 3, respectively. The perturbation amplitude is defined as half the difference in radius between bubbles and spikes. Figure 4 shows the time-varying dimensionless amplitudes of the inner interface (α_i) and outer interface (α_o) for the three experimental cases (see symbols). Time is scaled as $\tau = t\dot{R}_i/R_i^0$, and the amplitude is scaled as $\alpha_{i/o} = n(a_{i/o} - a_{i/o}^0)/R_{i/o}^0$. The uncertainty in the perturbation amplitude is ± 0.067 mm, and

https://doi.org/10.1017/jfm.2026.11885 Published online by Cambridge University Press

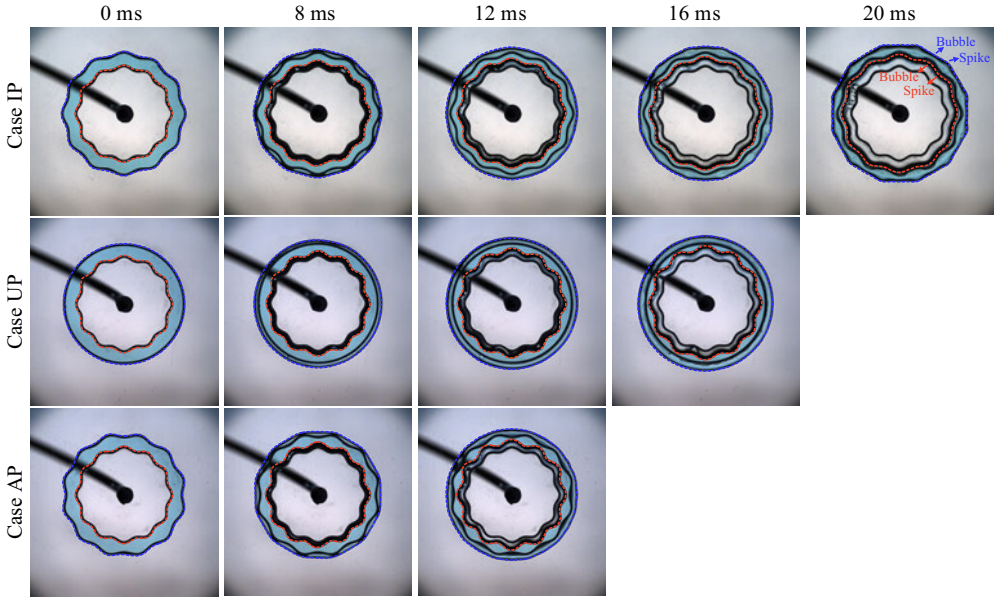


Figure 3. Evolution of a cylindrically divergent water layer under various initial conditions, where the outer edges of the inner and outer interfaces are marked with red and blue dashed lines, respectively.

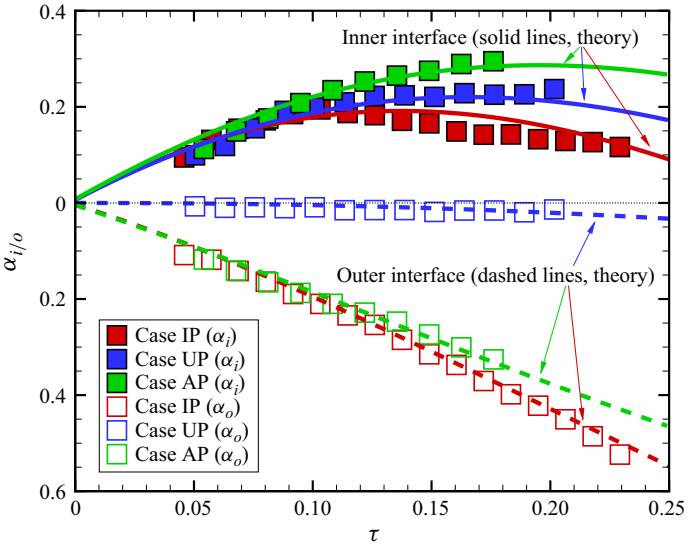


Figure 4. Time-varying dimensionless amplitudes of water–air interfaces in various cases. Symbols represent the experimental results, while solid and dashed lines represent the linear model predictions for the inner and outer interfaces, respectively.

the corresponding dimensionless amplitude has uncertainty approximately ± 0.03. These uncertainties are smaller than the symbol sizes in figure 4.

For the inner interface in the IP case, α_i grows continuously, peaks at $\tau \approx 0.1$, then decreases due to surface tension suppression (Liang & Luo 2025). In contrast, after $\tau \approx 0.1$, α_i remains nearly constant in the UP case, and increases slightly in the AP case. For the outer interface in the UP case, α_o grows slightly due to the weak feedthrough

https://doi.org/10.1017/jfm.2026.11885 Published online by Cambridge University Press

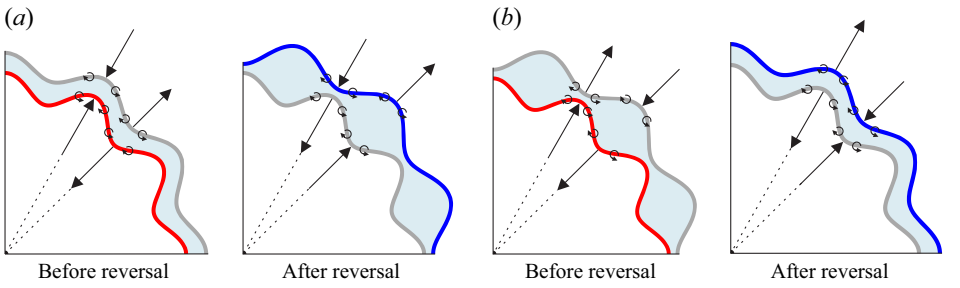


Figure 5. Sketch of the development of inner and outer interfaces before and after the reversal of the outer interface in cases (*a*) IP and (*b*) AP. Straight arrows illustrate the growth direction of the interface perturbation, and arcs with arrows illustrate the vorticity deposition.

between the two interfaces. In the IP and AP cases, α_o increases continuously, with the IP case showing a slightly higher α_o after $\tau \approx 0.1$. It is noted that the definition of the dimensionless amplitude causes α_o to grow from zero, making the phase reversal not directly evident, and leading to an apparent monotonic increase. Overall, the initial phase difference between the two interfaces has a non-negligible influence on the instability evolution, as explained in figure 5.

In the IP case, where the two interfaces are initially in-phase, before the perturbation on the outer interface reverses, the bubble/spike of the inner interface grows opposite to the spike/bubble of the outer interface. Because the water layer is incompressible, the outer interface suppresses perturbation growth on the inner interface. After the reversal of the outer interface, the bubble/spike of the inner interface grows in the same direction as that of the outer interface, so the inner interface promotes the growth of the outer interface. In contrast, in the AP case, where the two interfaces are initially anti-phase, before the reversal of the outer interface, the bubble/spike of the inner interface grows in the same direction as that of the outer interface; thus the outer interface promotes growth on the inner interface. After the reversal of the outer interface, the inner interface grows opposite to the outer interface, so the inner interface suppresses growth on the outer interface.

We consider a system of three incompressible, inviscid and initially irrotational fluids separated by two interfaces with small perturbations η_i and η_o (see (2.1)) in cylindrical geometry (Guo *et al.* 2017). The densities of the inner, middle and outer fluids are, respectively, ρ_1 $(0 < R < R_i)$, ρ_2 $(R_i < R < R_o)$ and ρ_3 $(R_o < R < \infty)$. A small single-mode perturbation on the inner interface (η_i) and outer interface (η_o) is written as

$$\eta_i(\theta, t) = R_i + a_i \cos(n\theta), \quad \eta_o(\theta, t) = R_o + a_o \cos(n\theta). \tag{3.1}$$

The velocity potentials for the inner fluid (ϕ_1), middle fluid (ϕ_2) and outer fluid (ϕ_3) satisfy the kinematic continuity condition for normal velocity components across the inner interface at $R = R_i$,

$$\frac{\partial \eta_i}{\partial t} + \frac{1}{R^2}\frac{\partial \eta_i}{\partial \theta}\frac{\partial \phi_1}{\partial \theta} - \frac{\partial \phi_1}{\partial R} = \frac{\partial \eta_i}{\partial t} + \frac{1}{R^2}\frac{\partial \eta_i}{\partial \theta}\frac{\partial \phi_2}{\partial \theta} - \frac{\partial \phi_2}{\partial R} = 0, \tag{3.2}$$

and across the outer interface at $R = R_o$,

$$\frac{\partial \eta_o}{\partial t} + \frac{1}{R^2}\frac{\partial \eta_o}{\partial \theta}\frac{\partial \phi_2}{\partial \theta} - \frac{\partial \phi_2}{\partial R} = \frac{\partial \eta_o}{\partial t} + \frac{1}{R^2}\frac{\partial \eta_o}{\partial \theta}\frac{\partial \phi_3}{\partial \theta} - \frac{\partial \phi_3}{\partial R} = 0. \tag{3.3}$$

https://doi.org/10.1017/jfm.2026.11885 Published online by Cambridge University Press

Then we can obtain the perturbed velocity potentials as

$$\phi_1 = d_1(t)\ R^n \cos(n\theta), \tag{3.4}$$

$$\phi_2 = [d_2(t)\ R^n + d_3(t)\ R^{-n}] \cos(n\theta), \tag{3.5}$$

$$\phi_3 = d_4(t)\ R^{-n} \cos(n\theta). \tag{3.6}$$

At the inner interface, normal stress continuity including surface tension (σ_i) yields

$$\begin{aligned} &-\rho_1 \left[\frac{\partial \phi_1}{\partial t} + \frac{1}{2} \left(\frac{\partial \phi_1}{\partial R} \right)^2 + \frac{1}{2R^2} \left(\frac{\partial \phi_1}{\partial \theta} \right)^2 + g R_i \right] + \sigma_i \kappa_i \\ &+\rho_2 \left[\frac{\partial \phi_2}{\partial t} + \frac{1}{2} \left(\frac{\partial \phi_2}{\partial R} \right)^2 + \frac{1}{2R^2} \left(\frac{\partial \phi_2}{\partial \theta} \right)^2 + g R_i \right] = 0. \end{aligned} \tag{3.7}$$

At the outer interface, normal stress continuity including surface tension (σ_o) yields:

$$\begin{aligned} &-\rho_2 \left[\frac{\partial \phi_2}{\partial t} + \frac{1}{2} \left(\frac{\partial \phi_2}{\partial R} \right)^2 + \frac{1}{2R^2} \left(\frac{\partial \phi_2}{\partial \theta} \right)^2 + g R_o \right] + \sigma_o \kappa_o \\ &+\rho_3 \left[\frac{\partial \phi_3}{\partial t} + \frac{1}{2} \left(\frac{\partial \phi_3}{\partial R} \right)^2 + \frac{1}{2R^2} \left(\frac{\partial \phi_3}{\partial \theta} \right)^2 + g R_o \right] = 0. \end{aligned} \tag{3.8}$$

The terms $(\partial\phi/\partial R)^2$ are of second order and are therefore neglected. The curvatures of the inner interface (κ_i) and outer interface (κ_o) can be approximated as

$$\kappa_i \approx \frac{1}{R_i} - \frac{a_i(n^2-1)\cos(n\theta)}{R_i^2}, \quad \kappa_o \approx \frac{1}{R_o} - \frac{a_o(n^2-1)\cos(n\theta)}{R_o^2}. \tag{3.9}$$

Collecting terms proportional to $\cos(n\theta)$ in (3.7) and (3.8) gives the governing equations for cylindrical RTI of successive interfaces considering surface tension:

$$\ddot{a}_i - \frac{(1+A_i)\zeta^{-n+1}}{1+A_i\zeta^{-2n}}\ddot{a}_o + 2\frac{\dot{R}_i}{R_i}\dot{a}_i - \frac{1-\zeta^{-2n}}{1+A_i\zeta^{-2n}}\left[\frac{nA_i g}{R_i} - \frac{\sigma_i(n^2-1)n}{(\rho_1+\rho_2)R_i^3}\right] a_i = 0, \tag{3.10}$$

$$\ddot{a}_o - \frac{(1-A_o)\zeta^{-n-1}}{1-A_o\zeta^{-2n}}\ddot{a}_i + 2\frac{\dot{R}_o}{R_o}\dot{a}_o - \frac{1-\zeta^{-2n}}{1-A_o\zeta^{-2n}}\left[\frac{nA_o g}{R_o} - \frac{\sigma_o(n^2-1)n}{(\rho_2+\rho_3)R_o^3}\right] a_o = 0, \tag{3.11}$$

with $\zeta = R_o/R_i$. The present model is consistent, in the incompressible, zero-acceleration, zero-surface-tension limit, with the linear model for thin-shell cylindrical RTI proposed by Yuan *et al.* (2024).

Figure 4 shows the linear theory predictions for the inner interface (solid lines) and outer interface (dashed lines). The initial amplitude growth rates of the inner and outer interfaces, $\dot{a}_i^0 = nA_i a_i^+ \dot{R}_i/R_i^0$ and $\dot{a}_o^0 = nA_o a_o^+ \dot{R}_o/R_o^0$, follow cylindrical RMI theory (Mikaelian 2005), where a_i^+ and a_o^+ are the suddenly-injected-flow compressed amplitudes of the inner and outer interfaces measured from experiments. The theoretical predictions agree well with experiments in all near-unity Atwood number cases, confirming that under $|A_i| = |A_o| = 1.0$ conditions: (i) when the two interfaces are initially in-phase, the feedthrough suppresses the instability on the inner interface and promotes it on

https://doi.org/10.1017/jfm.2026.11885 Published online by Cambridge University Press

the outer interface; (ii) when initially anti-phase, the feedthrough promotes the instability on the inner interface and suppresses it on the outer interface; and (iii) the inner interface instability in the case where the outer interface is initially unperturbed lies between the in-phase and anti-phase cases. A small but noticeable discrepancy is observed for the inner interface in the IP case at $\tau \approx 0.17$, where the experimental amplitude is slightly lower than the linear prediction. This deviation is likely caused by minor fluctuations in the injected air flow rate (approximately $\pm 2\,\%$ around the nominal $25\,\mathrm{l\,min^{-1}}$).

For cylindrical RTI, assuming exponential form for the perturbation amplitudes, (3.10) and (3.11) give the growth factors of the inner interface (γ_i) and outer interface (γ_o) satisfying

$$\gamma_i^2 - \frac{a_o^0}{a_i^0}\frac{(1+A_i)\zeta^{-n+1}}{1+A_i\zeta^{-2n}}\gamma_o^2 + 2\frac{\dot{R}_i}{R_i}\gamma_i - \frac{1-\zeta^{-2n}}{1+A_i\zeta^{-2n}}\left[\frac{nA_ig}{R_i} - \frac{\sigma_i(n^2-1)n}{(\rho_1+\rho_2)R_i^3}\right] = 0, \tag{3.12}$$

$$\gamma_o^2 - \frac{a_i^0}{a_o^0}\frac{(1-A_o)\zeta^{-n-1}}{1-A_o\zeta^{-2n}}\gamma_i^2 + 2\frac{\dot{R}_o}{R_o}\gamma_o - \frac{1-\zeta^{-2n}}{1-A_o\zeta^{-2n}}\left[\frac{nA_og}{R_o} - \frac{\sigma_o(n^2-1)n}{(\rho_2+\rho_3)R_o^3}\right] = 0. \tag{3.13}$$

Explicit expressions for γ_i and γ_o can only be achieved under the conditions $\dot{R}_i = \dot{R}_o = 0$. Physically, this condition corresponds to a quasi-static state where the mean radii of the interfaces do not change with time, i.e. the interfaces are stationary or the radial motion is momentarily zero. Under this condition, the expression for γ_i and γ_o can be derived as

$$\gamma_i^2 = \epsilon_i(\gamma_i^\infty)^2, \quad \gamma_o^2 = \epsilon_o(\gamma_o^\infty)^2, \tag{3.14}$$

where γ_i^∞ and γ_o^∞ represent the growth factors of the independent inner and outer interfaces ($\zeta \to \infty$), respectively:

$$(\gamma_i^\infty)^2 = \frac{nA_ig}{R_i} - \frac{\sigma_i(n^2-1)n}{(\rho_1+\rho_2)R_i^3}, \quad (\gamma_o^\infty)^2 = \frac{nA_og}{R_o} - \frac{\sigma_o(n^2-1)n}{(\rho_2+\rho_3)R_o^3}. \tag{3.15}$$

Here, ϵ_i and ϵ_o are the feedthrough efficiency factors of the inner and outer interfaces, respectively:

$$\epsilon_i = \frac{1-A_o\zeta^{-2n}}{1+A_iA_o\zeta^{-2n}} + \frac{a_o^0}{a_i^0}\frac{(1+A_i)\zeta^{-n+1}}{1+A_iA_o\zeta^{-2n}}\left(\frac{\gamma_o^\infty}{\gamma_i^\infty}\right)^2, \tag{3.16}$$

$$\epsilon_o = \frac{1+A_i\zeta^{-2n}}{1+A_iA_o\zeta^{-2n}} + \frac{a_i^0}{a_o^0}\frac{(1-A_o)\zeta^{-n-1}}{1+A_iA_o\zeta^{-2n}}\left(\frac{\gamma_i^\infty}{\gamma_o^\infty}\right)^2. \tag{3.17}$$

The feedthrough efficiency factors ϵ_i and ϵ_o are defined as the ratios $\gamma_i^2/(\gamma_i^\infty)^2$ and $\gamma_o^2/(\gamma_o^\infty)^2$. This definition is natural: efficiency 1 corresponds to no feedthrough (the growth rate equals that of an independent interface); values different from 1 indicate that coupling either enhances ($\epsilon > 1$) or suppresses ($\epsilon < 1$) the instability relative to the independent case. Since $\epsilon_i > 0$ and $\epsilon_o > 0$, the perturbation growth trend of the two successive interfaces is solely determined by the instability growth of the independent inner and outer interfaces: if $[nA_ig/R_i - (\sigma_i(n^2-1)n)/((\rho_1+\rho_2)R_i^3)] < 0$ for the inner interface (or $[nA_og/R_o - (\sigma_o(n^2-1)n)/((\rho_1+\rho_2)R_o^3)] < 0$ for the outer interface), then the perturbation growth presents an oscillatory solution; if it equals zero, then we have a freeze-out solution; if it is positive, then we have an unstable solution. Because the

https://doi.org/10.1017/jfm.2026.11885 Published online by Cambridge University Press

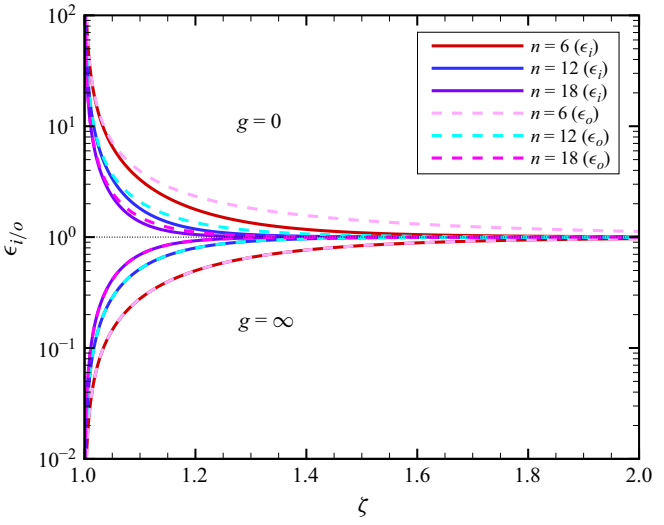


Figure 6. Feedthrough efficiency factors ϵ_i and ϵ_o versus radius ratio ζ for various azimuthal wavenumber n under $A_i = 1.0$, $A_o = -1.0$, $a_i = a_o$ and $\sigma_i = \sigma_o$ conditions.

interface acceleration achievable in the laboratory is limited or even zero (as in the present study), the oscillatory solution is observed in our experiments (e.g. case IP in figure 4).

Now we discuss the influence of physical parameters such as the radius ratio of two interfaces, interface acceleration, perturbation wavenumber on the feedthrough between the two interfaces according to (3.16) and (3.17) under near-unity Atwood number ($A_i = 1.0$, $A_o = -1.0$), same initial perturbation amplitude ($a_i^0 = a_o^0$) and same surface tension coefficient ($\sigma_i = \sigma_o$) conditions. First, for the zero acceleration case $g = 0$, the feedthrough efficiency factors reduce to

$$\epsilon_i|_{g=0} = \frac{1 + \zeta^{-2n} + 2\zeta^{-n-2}}{1 - \zeta^{-2n}}, \quad \epsilon_o|_{g=0} = \frac{1 + \zeta^{-2n} + 2\zeta^{-n+2}}{1 - \zeta^{-2n}}. \tag{3.18}$$

Second, for an extremely large acceleration case (e.g. ICF and supernovae) where $g \to \infty$, the feedthrough efficiency factors reduce to

$$\epsilon_i|_{g\to\infty} = \epsilon_o|_{g\to\infty} = \frac{1 + \zeta^{-2n} - 2\zeta^{-n}}{1 - \zeta^{-2n}}. \tag{3.19}$$

Figure 6 shows the variation of ϵ_i and ϵ_o versus ζ in the range 1.0–2.0, for $g = 0$ and $g \to \infty$. As $\zeta \to 1$, the feedthrough strength between the two interfaces increases, making the two interfaces more unstable under $g = 0$ (since $\epsilon_i > 1$ and $\epsilon_o > 1$), but more stable under $g \to \infty$ (since $\epsilon_i < 1$ and $\epsilon_o < 1$). Moreover, as the azimuthal wavenumber n increases, the values of ϵ_i and ϵ_o approach 1.0, indicating weaker feedthrough. Furthermore, the feedthrough effect on the outer interface is stronger than that on the inner interface under $g = 0$, and the difference diminishes as n increases. In contrast, under $g \to \infty$, the feedthrough effect is the same for both interfaces. It is encouraging to see that the feedthrough suppresses instabilities on both interfaces under $g \to \infty$ conditions, especially at lower wavenumbers. This is crucial for ICF experiments, where suppressing hydrodynamic instability is key to minimising mixing between the hot fuel and the cold pusher, and improving nuclear ignition efficiency.

The predictions in figure 6 are derived from the linear theory under the quasi-static assumption and the additional simplifications listed above. While the theory itself has

https://doi.org/10.1017/jfm.2026.11885 Published online by Cambridge University Press

been validated against our experiments for the near-unity Atwood number regime, the specific quantitative trends for ϵ_i and ϵ_o versus ζ in the limits $g = 0$ and $g \to \infty$ have not been experimentally verified in the present study. Moreover, in actual ICF or supernova environments, compressibility, turbulence and nonlinear effects would modify the evolution; therefore, the present results should be interpreted as a qualitative trend rather than a quantitative prediction for those extreme conditions.

4. Conclusions

This study systematically examines the feedthrough between two successive cylindrical water–air interfaces in a cylindrically divergent (outward-expanding) geometry. Hydrophobic-coated rings are used to generate a water layer with controllable initial conditions. A linear model coupling the inner and outer perturbations is developed and validated against high-resolution experiments in the near-unity Atwood number regime.

The initial phase difference between the two interfaces profoundly alters the direction of feedthrough. In the initially in-phase (IP) case, the outer interface suppresses the inner perturbation before the outer interface reverses, but the inner interface promotes the outer perturbation afterwards. In the initially anti-phase (AP) case, the outer interface promotes the inner perturbation before reversal, but the inner interface suppresses the outer perturbation afterwards. The inner interface growth in the initially unperturbed outer interface (UP) case lies intermediate between the IP and AP cases. The agreement between theory and experiment demonstrates that the linear coupling model captures the essential physics of feedthrough in layered flows.

The derived feedthrough efficiency factors ϵ_i and ϵ_o show that the coupling strength depends on various physical parameters. Under zero acceleration ($g = 0$, as in the present experiments), the feedthrough enhances instabilities on both interfaces. In contrast, under extremely high acceleration ($g \to \infty$, relevant to ICF), the feedthrough might suppress instabilities on both interfaces, with stronger suppression at lower wavenumbers. This suppression, if qualitatively applicable, might be relevant for ICF target design, as it may minimise fuel-pusher mixing and help to maintain temperature stratification. These results provide critical new insights into hydrodynamic instabilities in both radially convergent (e.g. ICF) and radially divergent (e.g. supernova) geometries.

Funding. This work was supported by the Natural Science Foundation of China (12572256, 12388101, 12441203 and 24FAA00998) and the Chinese Academy of Sciences Project for Young Scientists in Basic Research (grant no. YSBR-132).

Declaration of interests. The authors report no conflict of interest.

Appendix. Surface tension effects

To quantify the role of surface tension, which lies in the transitional Weber number regime ($We = 2-5$), we used our linear model to compute the interface amplitudes of both inner and outer interfaces in the three cases with surface tension set to zero, as shown in figure 7. Without surface tension, the amplitudes of the inner interfaces grow monotonically and do not exhibit the peak and subsequent decrease observed in the experiment. Surface tension suppresses the growth of the inner interface after $\tau \approx 0.05$. In contrast, under zero surface tension conditions, the dimensionless amplitude growth of the outer interface slightly decreases because of weaker feedthrough from the inner interface to the outer interface. These results demonstrate that surface tension plays a significant, non-negligible role in our experiments, especially in suppressing the inner interface instability.

https://doi.org/10.1017/jfm.2026.11885 Published online by Cambridge University Press

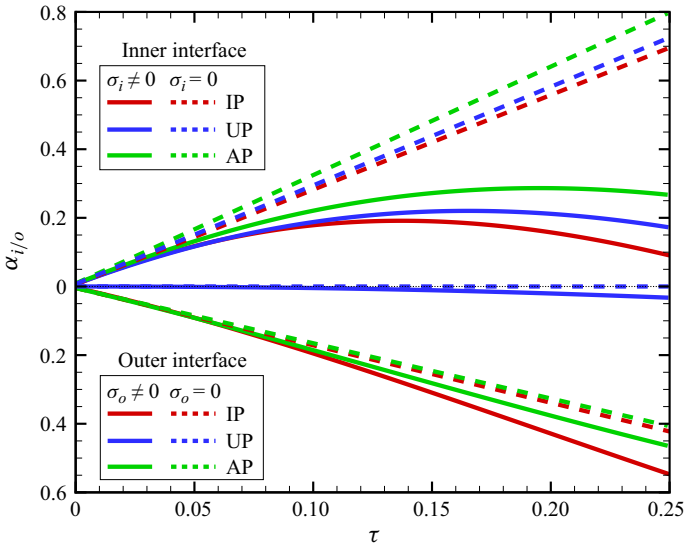


Figure 7. Time-varying dimensionless amplitudes of the water–air interfaces predicted by the linear models. Solid and dashed lines denote predictions with and without surface tension, respectively.

References

Bell, G.I. 1951 Taylor instability on cylinders and spheres in the small amplitude approximation. *Tech. Rep.* No. LA-1321. Los Alamos National Laboratory.

Ding, J., Si, T., Yang, J., Lu, X., Zhai, Z. & Luo, X. 2017 Measurement of a Richtmyer–Meshkov instability at an air–SF_6 interface in a semiannular shock tube. *Phys. Rev. Lett.* **119** (1), 014501.

Epstein, R. 2004 On the Bell–Plesset effects: the effects of uniform compression and geometrical convergence on the classical Rayleigh–Taylor instability. *Phys. Plasmas* **11** (11), 5114–5124.

Goncharov, V.N., McKenty, P., Skupsky, S., Betti, R., McCrory, R.L. & Cherfils-Clérouin, C. 2000 Modeling hydrodynamic instabilities in inertial confinement fusion targets. *Phys. Plasmas* **7** (12), 5118–5139.

Guo, H., Wang, L., Ye, W., Wu, J. & Zhang, W. 2017 Rayleigh–Taylor instability of multi-fluid layers in cylindrical geometry. *Chin. Phys. B* **26** (12), 125202.

Hsiang, L.-P. & Faeth, G.M. 1992 Near-limit drop deformation and secondary breakup. *Intl J. Multiphase Flow* **18** (5), 635–652.

Liang, Y. & Luo, X. 2025 Experimental investigation of cylindrically divergent Rayleigh–Taylor instability on a water–air interface. *J. Fluid Mech.* **1016**, R2.

Liang, Y. & Luo, X. 2026 Viscosity contrast destabilises radial Rayleigh–Taylor flow. *J. Fluid Mech.* **1028**, R2.

Lindl, J., Landen, O., Edwards, J., Moses, E. & NIC Team 2014 Review of the National Ignition Campaign 2009–2012. *Phys. Plasmas* **21** (2), 020501.

Merritt, E.C., Doss, F.W., Levesque, J.M., Rasmus, A.M., Desjardins, T., Di Stefano, C.A., Flippo, K.A. & Schmidt, D.W. 2024 Quantitative radiography for determining density fluctuations in HED experiments. *Rev. Sci. Instrum.* **95** (12), 123511.

Mikaelian, K.O. 1982*a* Normal modes and symmetries of the Rayleigh–Taylor instability in stratified fluids. *Phys. Rev. Lett.* **48** (19), 1365.

Mikaelian, K.O. 1982*b* Rayleigh–Taylor instabilities in stratified fluids. *Phys. Rev. A* **26** (4), 2140.

Mikaelian, K.O. 2005 Rayleigh–Taylor and Richtmyer–Meshkov instabilities and mixing in stratified cylindrical shells. *Phys. Fluids* **17**, 094105.

Mikaelian, K.O. 2025 Feedthrough and suppression of Rayleigh–Taylor and Richtmyer–Meshkov instabilities. *Phys. Fluids* **37** (3), 032114.

Müller, B. 2020 Hydrodynamics of core-collapse supernovae and their progenitors. *Living Rev. Comput. Astrophys.* **6**, 3.

Plesset, M.S. 1954 On the stability of fluid flows with spherical symmetry. *J. Appl. Phys.* **25**, 96–98.

https://doi.org/10.1017/jfm.2026.11885 Published online by Cambridge University Press

RAYLEIGH, LORD 1833 Investigation of the character of the equilibrium of an incompressible heavy fluid of variable density. *Proc. Lond. Math. Soc.* **14**, 170–177.

RYUTOV, D.D. & DORF, M.A. 2014 Evolution of helical perturbations in a thin-shell model of an imploding liner. *Phys. Plasmas* **21** (11), 112704.

SAUPPE, J.P. *et al.* 2020 Demonstration of scale-invariant Rayleigh–Taylor instability growth in laser-driven cylindrical implosion experiments. *Phys. Rev. Lett.* **124**, 185003.

TAYLOR, G. 1950 The instability of liquid surfaces when accelerated in a direction perpendicular to their planes. I. *Proc. R. Soc. Lond. A* **201** (1065), 192–196.

WALCHLI, B. & THORNBER, B. 2017 Reynolds number effects on the single-mode Richtmyer–Meshkov instability. *Phys. Rev. E* **95** (1), 013104.

WANG, L., GUO, H., WU, J., YE, W., LIU, J., ZHANG, W. & HE, X. 2014 Weakly nonlinear Rayleigh–Taylor instability of a finite-thickness fluid layer. *Phys. Plasmas* **21** (12), 122710.

WEIR, S.T., CHANDLER, E.A. & GOODWIN, B.T. 1998 Rayleigh–Taylor instability experiments examining feedthrough growth in an incompressible, convergent geometry. *Phys. Rev. Lett.* **80** (17), 3763.

WEIS, M.R., ZHANG, P., LAU, Y.Y., SCHMIT, P.F., PETERSON, K.J., HESS, M. & GILGENBACH, R.M. 2015 Coupling of sausage, kink, and magneto-Rayleigh–Taylor instabilities in a cylindrical liner. *Phys. Plasmas* **22** (3), 032706.

YUAN, M., ZHAO, Z., LIU, L., WANG, P., LIU, N. & LU, X. 2023 Instability evolution of a shock-accelerated thin heavy fluid layer in cylindrical geometry. *J. Fluid Mech.* **969**, A6.

YUAN, M., ZHAO, Z., LIU, L., WANG, P., LIU, N. & LU, X. 2024 Instability evolution on a shock-accelerated cylindrical fluid layer with arbitrary atwood numbers. *J. Fluid Mech.* **1000**, A9.

ZHOU, Y., SADLER, J.D. & HURRICANE, O.A. 2025 Instabilities and mixing in inertial confinement fusion. *Annu. Rev. Fluid Mech.* **57**, 197–225.

https://doi.org/10.1017/jfm.2026.11885 Published online by Cambridge University Press